

Effect of Digital Elevation Model Resolution on the Simulation of the Snow Cover Evolution in the High Atlas

Mohamed Wassim Baba, Simon Gascoin, Christophe Kinnard, Ahmed Marchane, Lahoucine Hanich, Mohamed Wassim Baba

▶ **To cite this version:**

Mohamed Wassim Baba, Simon Gascoin, Christophe Kinnard, Ahmed Marchane, Lahoucine Hanich, et al.. Effect of Digital Elevation Model Resolution on the Simulation of the Snow Cover Evolution in the High Atlas. Water Resources Research, 2019, 55 (7), pp.5360 - 5378. 10.1029/2018WR023789 . hal-02181441

HAL Id: hal-02181441
https://hal.science/hal-02181441

Submitted on 12 Jul 2019

HAL is a multi-disciplinary open access archive for the deposit and dissemination of scientific research documents, whether they are published or not. The documents may come from teaching and research institutions in France or abroad, or from public or private research centers.

L'archive ouverte pluridisciplinaire **HAL**, est destinée au dépôt et à la diffusion de documents scientifiques de niveau recherche, publiés ou non, émanant des établissements d'enseignement et de recherche français ou étrangers, des laboratoires publics ou privés.



Distributed under a Creative Commons Attribution - NonCommercial - NoDerivatives 4.0 International License

Water Resources Research

RESEARCH ARTICLE
10.1029/2018WR023789

Special Section:
Advances in remote sensing, measurement, and simulation of seasonal snow

Effect of Digital Elevation Model Resolution on the Simulation of the Snow Cover Evolution in the High Atlas

Mohamed Wassim Baba[1], Simon Gascoin[1], Christophe Kinnard[2], Ahmed Marchane[3], and Lahoucine Hanich[3]

[1]Centre d'Etudes Spatiales de la Biosphère, Université de Toulouse, CNRS/CNES/INRA/IRD/UPS, Toulouse, France, [2]Centre de recherche sur les interactions bassin versants-écosystémes aquatiques (RIVE), Université du Québec à Trois-Rivières, Trois-Rivières, Quebec, Canada, [3]Laboratoire de Géoressources - Unité associée au CNRST (URAC42), Département des Sciences de la Terre, Faculté des Sciences et Techniques, Université Cadi Ayyad, Marrakech, Morocco

Key Points:
- A distributed energy balance snow model is applied in the High Atlas for the first time
- The model performance decreases at resolution coarser than 250 m
- This result is consistent with the semivariogram of the topographic slope

Supporting Information:
- Supporting Information S1

Correspondence to:
S. Gascoin,
simon.gascoin@cesbio.cnes.fr

Citation:
Baba, M. W., Gascoin, S., Kinnard, C., Marchane, A., & Hanich, L. (2019). Effect of digital elevation model resolution on the simulation of the snow cover evolution in the High Atlas. *Water Resources Research*, *55*. https://doi.org/10.1029/2018WR023789

Received 30 JUL 2018
Accepted 18 APR 2019
Accepted article online 9 MAY 2019

©2019. The Authors.
This is an open access article under the terms of the Creative Commons Attribution-NonCommercial-NoDerivs License, which permits use and distribution in any medium, provided the original work is properly cited, the use is non-commercial and no modifications or adaptations are made.

Abstract The snow melt from the High Atlas represents a crucial water resource for crop irrigation in the semiarid regions of Morocco. Recent studies have used assimilation of snow cover area data from high-resolution optical sensors to compute the snow water equivalent and snow melt in other mountain regions. These techniques however require large model ensembles, and therefore it is a challenge to determine the adequate model resolution that yields accurate results with reasonable computation time. Here we study the sensitivity of an energy balance model to the resolution of the model grid for a pilot catchment in the High Atlas. We used a time series of 8-m resolution snow cover area maps with an average revisit time of 7.5 days to evaluate the model results. The digital elevation model was generated from Pléiades stereo images and resampled from 8 to 30, 90, 250, 500, and 1,000 m. The results indicate that the model performs well from 8 to 250 m but the agreement with observations drops at 500 m. This is because significant features of the topography were too smoothed out to properly characterize the spatial variability of meteorological forcing, including solar radiation. We conclude that a resolution of 250 m might be sufficient in this area. This result is consistent with the shape of the semivariogram of the topographic slope, suggesting that this semivariogram analysis could be used to transpose our conclusion to other study regions.

1. Introduction

In many semiarid and Mediterranean catchments, snow melt runoff is an essential water resource for farmers who need to irrigate their crops during the dry summer season (Fayad et al., 2017; Viviroli et al., 2007). In the Tensift region of Morocco near Marrakech, the major rivers have their headwaters in the High Atlas Mountains. The contribution of snow melt to their mean annual discharge was estimated to range from 15% to 45% (Boudhar et al., 2009). However, this contribution is probably more important from a water resource management perspective because (i) the annual flood due to snow melt occurs at this period of the year when irrigation is crucial to the crop growth and (ii) the melt water flood is more stable and easier to use than the flash floods triggered by heavy rainfalls, which often cause more harm than good in this region (Zkhiri et al., 2017).

The analysis of optical remote sensing data showed that the snow cover in the High Atlas is characterized by high spatial and temporal variability (Boudhar et al., 2010; Chaponniere et al., 2005; Marchane et al., 2014). However, these studies did not address the variability of the snow water equivalent (SWE) and snow melt, which are the main variables of interest for hydrologists and water managers. The variability of the SWE and snow melt was analyzed at the point scale using energy balance models forced by meteorological station data (Boudhar et al., 2016; López-Moreno et al., 2017; Schulz & De Jong, 2004). The important results of these studies are that the main source of energy for melting is net radiation and that snow sublimation can be significant but with a high interannual variability. Computed sublimation ranged between 7% and 25% of the total ablation at Oukaimden (3,230 m) on the windward slope of the High Atlas, while it reached 45% at Tichki (3,260 m) on the drier, leeside of the High Atlas. These point-scale modeling studies, however, did not allow the computation of melt rates at the catchment scale. To our best knowledge, the only attempts to compute the snow melt at catchment scale in the High Atlas were based on degree day models (Boudhar

et al., 2009, 2013). Yet, the aforementioned point-scale modeling studies suggest that distributed energy balance models should be more suitable to capture the processes driving the evolution of the snowpack in the High Atlas area since the standard degree day approach does not explicitly include the radiation and neglects sublimation. A drawback of distributed energy balance models is that they require more input forcing data than simpler, empirical models. In the mountainous areas of Morocco, the in situ network of meteorological stations is extremely sparse, while the spatial variability of the climate is exacerbated by the complex topography of the terrain. The errors caused by the large uncertainties in the input data can spread over the course of a snow season due to the temporal persistence of the snowpack properties and cause significant biases in the SWE and snow melt (Durand et al., 2008).

The recent surge of high-resolution remote sensing data, for example, the distribution of the entire Landsat archive and the advent of the Sentinel-2 mission, have opened new avenues to the field of snow hydrology in semiarid and Mediterranean regions (Fayad et al., 2017). These data are free and enable mapping of the snow cover extent with a spatial resolution (20 to 30 m) which is compatible with the variability of the snow cover in semiarid regions. For instance, it enables capturing of the large differences in snow cover area (SCA) due to the contrasted melt rates between north and south facing slopes (Pimentel et al., 2017a). A limitation to the Landsat mission for snow cover applications is the low frequency of observation (Landsat-8 mission has a revisit time of 16 days). However, with Sentinel-2 the revisit time will be 5 days globally. In addition, the cloud cover in semiarid regions is more limited than in temperate regions. Thus, the main limitation is rather that Landsat-8 and Sentinel-2 are optical sensors and hence do not allow retrieving the internal snowpack properties such as the SWE and melt rates. This is why these data must be combined with a snowpack model through the calibration of the model parameters or within a data assimilation framework which accounts for the model and observation errors. This approach is considered superior to approaches based on passive microwave remote sensing to estimate the SWE in semiarid and Mediterranean mountain regions (Dozier et al., 2016). For instance, the assimilation of Moderate Resolution Imaging Spectroradiometer (MODIS) and Landsat SCA enabled reducing of the bias in the simulated SWE by 49% in the Rio Grande headwaters (USA; Durand et al., 2008). More recently, the assimilation of Landsat SCA into a distributed energy balance model was used to reconstruct the SWE in the California Sierra Nevada and the subtropical Andes (Margulis et al., 2015). The updated SWE estimation reduced the bias between modeled SWE and snow course by 60% to 82%.

These studies suggest that the assimilation of high-resolution SCA maps in a distributed snow cover energy balance model is a promising approach to improve our knowledge of the snow resource in the High Atlas. However, we lack perspectives on the applicability of this method since a snow cover energy balance model has never been applied in the Atlas Mountains, even without data assimilation (i.e., in an open loop). In particular, an important question before implementing a distributed data assimilation scheme is What is an adequate model spatial resolution?

In theory, the highest model resolution should provide the best results since the spatial variability of the SWE in mountains is strongly linked to the topographic variability (Molotch et al., 2005). Key factors are the dependence of precipitation and temperature on elevation, the effect of slope and aspect on incoming solar radiation, and the deflection of the wind field by the terrain (Barry, 1992; Jost et al., 2007). In addition, higher-resolution digital elevation models (DEMs) may more accurately reflect late-lying snow patches than lower-resolution DEM simulations. Melt water from these snow patches can be critical to sustain streamflow during the summer (Freudiger et al., 2017). Previous numerical experiments suggest that the mean SWE simulated by a distributed snowpack can decrease by 10% by changing the model grid resolution from 25 to 1,000 m (Schlögl et al., 2016). In the High Atlas, our field experience suggests that the model should at least resolve the hillslope scale, that is, a spatial scale with an order of magnitude of 10^2 m (Figure 1).

While higher spatial resolution are expected to better capture the variability of the snow cover, this is at the expense of the computational cost. Evaluating the computation time of the model is crucial in the perspective of data assimilation, which requires a large number of model runs. Margulis et al. (2015) used a model grid size of 90 m based on literature values (Blöschl, 1999; Winstral & Marks, 2014) but did not assess the impact of this choice on their results. Recently, Baldo and Margulis (2017) developed a multiresolution approach to optimize the computational cost, while preserving the necessary resolution for fine-scale snow processes. This scheme is based on a physiographic complexity metric snow modeling scheme and was



Figure 1. Photograph taken near Oukaimeden in the Rheraya catchment on 14 December 2016 (31.194°N, −7.584°S). It illustrates the effect of slope and aspect on the snow cover area at decametric scales that is often observed in the High Atlas.

evaluated with respect to a reference simulation at high resolution. However, the results of the new scheme were not compared to observations.

Other strategies (than changing the model grid resolution) were proposed to account for terrain heterogeneity on topographic-driven meteorological forcing while keeping low computational requirements. These approaches can be classified into two categories: (i) the subgrid approach (Essery & Marks, 2007; Gagnon et al., 2013; Müller & Scherer, 2005) and (ii) the semidistributed approach (Revuelto et al., 2017; Younas et al., 2017). The first approach was used to represent forcing variables as probabilistic distributions (instead of a single mean value) at the grid cell scale. This approach was mainly developed for land surface schemes (Arola & Lettenmaier, 1996; Essery & Marks, 2007), motivated by the fact that these models are designed to provide lower boundary conditions to regional and global climate models, which have kilometer resolution at best. To our best knowledge, however, there is no study which put together all forcing variables (radiation, wind, temperature, etc.) as subgrid processes to run a snowpack energy balance model in alpine terrain. The second option aims to explicitly resolve the effect of topography on predefined classes of topography. It has been notably used by Météo-France for operational avalanche forecasting and was recently implemented in the Canadian Land Surface Scheme (Younas et al., 2017). However, this approach is not practical to assimilate remote sensing observations which are distributed on a regular grid. In that perspective, it is more straightforward to run the model on a distributed grid. This also permits to explicitly represent snow redistribution processes such as the wind transport or avalanches (Revuelto et al., 2017).

The objective of this study is to determine an adequate model resolution to simulate the snow cover evolution in the semiarid context of the Atlas Mountains. We focus on a snow-dominated pilot catchment in the Atlas Mountains, where forcing and evaluation data are available. We adopted a practical approach; that is, we sought the lowest resolution which did not deteriorate the model performances. According to Blöschl (1999) the processes that influence the snowpack variability across the landscape have correlation lengths ranging from 1 m (wind drift) to 10 km (climatic conditions), while the effect of solar radiation at hillslopes of different aspects has a typical process scale of 100 m. Hence, we generated DEMs with resolutions of 8, 30, 90, 250, 500, and 1,000 m of the catchment using Pléiades stereoscopic imagery. These DEMs were used to assess from which resolution the model deteriorates too much with respect to observations. The simulations were done with SnowModel (Liston & Elder, 2006a), a distributed snow evolution model that was already tested in various regions, including semiarid mountains (e.g., Gascoin et al., 2013). Evaluation data include continuous snow depth measurements from an automatic weather station, but the model evaluation mainly relies on a time series of 8-m resolution SCA maps derived from Formosat-2 acquisitions during the 2008–2009 snow season. These Formosat-2 data can be seen as a surrogate of the Sentinel-2 data (the operational revisit frequency of 5 days was achieved in the Atlas during the 2017/2018 snow season). The accuracy of the simulations is balanced with the computation time. Finally, we investigate the consistency of the model results with the spatial variability of the topography in the study area, which allows us to propose a potential method to help determine the adequate model resolution to run an energy balance model beyond this particular location. To our best knowledge this study is the first to study the effect on model grid resolution based on in situ and high-resolution remote sensing observations in a semiarid mountainous environment. It is also the first evaluation of a distributed energy balance model in the High Atlas.

2. Study Area and Data

2.1. Study Area

We focus on the Rheraya catchment located in the High Atlas range (31.18°N, 7.86°W, Figure 1). The catchment area is 220 km^2, and its elevation ranges from 1,000 to 4,167 m above sea level (asl; Toubkal, highest peak in North Africa). This catchment is characterized by a semiarid climate, with irregular precipitation. Snow accumulation generally occurs above 1,500 m asl between December and March, and the melt season ends in June (Boudhar et al., 2007) . However, melt events are not uncommon in winter (Marchane et al., 2015). The Rheraya catchment was selected because it is a pilot site of the Tensift observatory, which is coor-

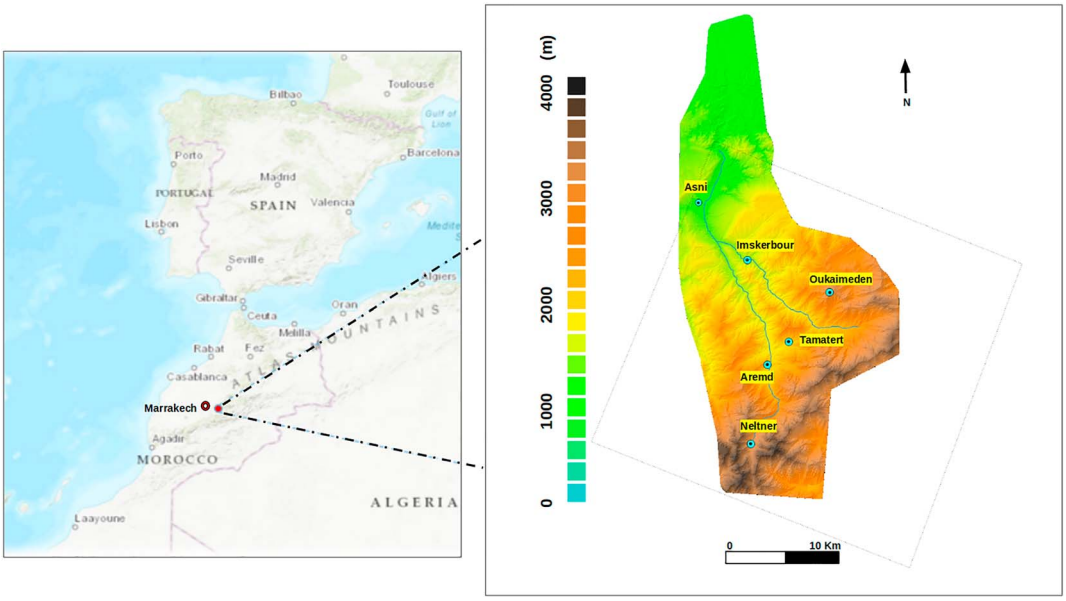


Figure 2. Map of the study area. The map on the right shows the digital elevation model derived from Pléiades stereo images over the Rheraya catchment, the extent of the Formosat-2 acquisitions, and the location of the Automatic Weather Stations.

dinated by the joint international laboratory Télédétection et Ressources en Eau en Méditerranée semi-Aride (TREMA) (Jarlan et al., 2015) within the framework of French-Moroccan cooperation. A number of meteorological stations were set up in the Rheraya catchment since 2003, including two high-elevation stations (see section 2.2.1). These stations provide critical data in this region where the meteorological network is otherwise extremely sparse (section 1). In addition, the Rheraya river is by itself an important tributary of the Tensift river, which runs through the even more arid Haouz plain and the city of Marrakech (currently about one million inhabitants in the metropolitan area, Figure 2). However, only a very low fraction of the runoff reaches Marrakech since most of the runoff from the headwater catchments such as the Rheraya feeds the Haouz aquifer by infiltration in the river bed or is diverted for irrigation between the mountains foothills and the city. The Haouz aquifer is the main source of water for irrigation and human consumption in the region.

2.2. Data

2.2.1. Meteorological Forcing

We used hourly meteorological data from four Automatic Weather Stations (AWS). These stations provide standard meteorological variables (Table 1), and the snow depth was recorded at Oukaimeden AWS using an acoustic snow gauge (Boudhar et al., 2016).

Table 1
Description of the Rheraya Automatic Weather Stations

Stationq	Coordinates (WGS-84)	Elevation (m)	Available data
Aremd	(31.124°N, −7.920°E)	1,965	T, RH, P, SR
Imskerbour	(31.205°N, −7.938°E)	1,404	T, RH, P
Neltner	(31.064°N, −7.938°E)	3,207	T, RH
Oukaimeden	(31.180°N, −7.865°E)	3,230	T, RH, P, SD
Tamatert	(31.142°N, −7.904°E)	1,924	P
Asni	(31.248°N, −7.980°E)	1,170	P

Note. The7 study period is from 1 November 2008 to 10 June 2009. T = temperature; P = precipitation; RH = relative humidity; SR = solar radiation; SD = snow depth.

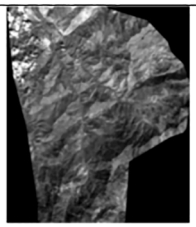
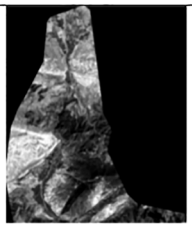
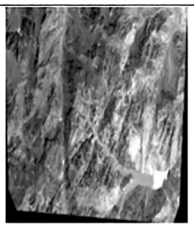
Zone	1	2	3
Plateform	1A	1B	1B
Acquisition date	2015-08-18 11:19:11 2015-08-18 11:19:39	2015-08-04 11:26:37 2015-08-04 11:27:07	2015-08-17 11:27:40 2015-08-17 11:28:08
Preview			
B/H	0.3	0.32	0.35

Figure 3. Characteristics of the Pléiades images. For each site, base-to-height ratio (B/H), the ratio of the distance between two successive positions of the satellite to its height above ground, is an indicator of the sensitivity to topography.

All these stations were installed during the early phase of the SUDMED project between 2002 and 2004 (Chehbouni et al., 2008) and were maintained as part of the Tensift observatory by the staff of the joint international laboratory TREMA (Jarlan et al., 2015). Only Oukaimeden station is equipped with a wind-sheltered Geonor T-200B precipitation gauge. The other stations (Aremd, Imskerbour, Tamatert, and Asni) have tipping bucket rain gauges. However, these stations rarely receive snow in contrast to Oukaimeden station. The instruments at Oukaimeden were described and by Boudhar et al. (2016) who used the data to evaluate the energy fluxes at the station. The station is located near the summit of a peak and just outside of a ski run on a gentle north facing slope (supporting information Figure S1).

2.2.2. DEM and Orthoimage

A DEM of 4-m resolution was produced for this study specifically. It was derived from Pléiades stereoscopic imagery. The Pléiades system is a constellation of two identical satellites (named Pléiades 1A and 1B). Both platforms are on the same near-polar Sun-synchronous orbit at 694 km of altitude and can acquire images at 70-cm resolution in the panchromatic band (480–830 nm). Due to its agility Pléiades can acquire two images of the same area with different angles along the same orbit. These stereoscopic images can be combined to derive a DEM. Pléiades spatial resolution is initially equal to 70 cm, but the images are provided at 50 cm after preprocessing.

We obtained three Pléiades stereo pairs covering the Rheraya catchment. These stereo pairs were acquired on 4 August 2015, 17 August 2015, and 18 August 2015 (Figure 3). The acquisition dates were constrained to summer to avoid the presence of snow. The images of 18 August 2015 are partly covered by clouds near their western edge. The base to height ratios (B/H) were respectively 0.32, 0.35, and 0.3 for each date. B/H ratios lower than 0.4 are recommended for mountainous terrain(Hasegawa et al., 2000). The operator (Airbus Space and Defense) provides a Rational Polynomial Coefficient (RPC) file with each image to allow the geolocalization of the images. These images and associated RPC files were used to generate a high-resolution DEM with the Ames Stereo Pipeline (ASP, version: 2.5), an open source stereogrammetry software developed by NASA (Shean et al., 2016), which supports Pléiades data and is efficient in mountainous regions (Marti et al., 2016). We applied the following workflow based on ASP command line utilities:

1. Alignment: In mountainous regions classical correlation which consists of matching analog pixels based on the RPC georeferencing only may fail due to sharp relief. Hence, we preprojected the right and left Pléiades images on the Shuttle Radar Topography Mission (SRTM1) DEM before aligning each pair separately using the `map project` command.
2. Stereoscopy: This step consisted of generating point clouds from stereoscopic pairs using the stereo command.
3. Rasterization: The three-point clouds were rasterized to grids of 4-m resolution through the `point2dem` command.
4. Mosaicing and blending: The three DEMs were merged using the `dem_mosaic` command.
5. Gap-filling of cloud covered area: In cloudy areas we obtained no-data values because the stereo correlation failed in the previous step. We filled these gaps by merging the Pléiades DEM with the SRTM DEM. This was done by resampling the SRTM DEM to 4-m resolution by cubic interpolation. Then, we merged

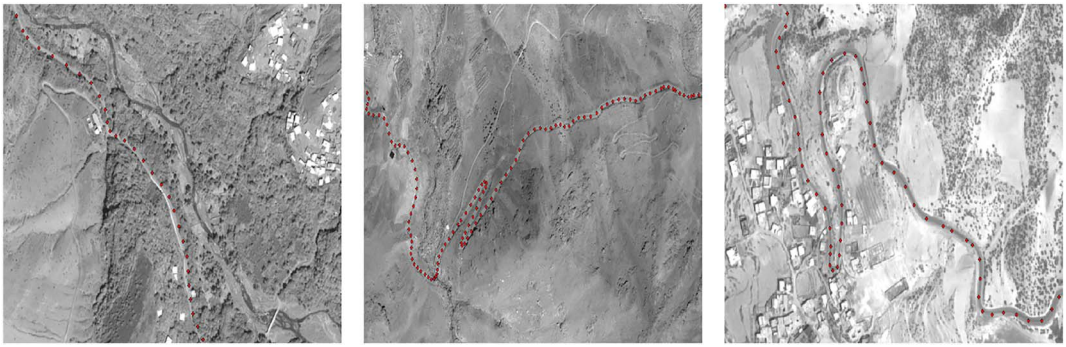


Figure 4. Comparison of the control points (red dots) and the orthoimage.

both DEMs using the `dem_mosaic` command again but with a priority blending length option which gives priority to the Pleiades DEM.

6. Orthoimage: Once the DEM is complete, we used it to orthorectify the panchromatic images at 1-m resolution in the WGS-84 UTM 29N spatial reference system. This orthoimages will thereafter allow us to validate horizontal accuracy of the DEM.
7. Filtering and gap-filling of artifacts: Using a hill-shaded version of the DEM and by loading the DEM in a 3-D visualization application, we identified obvious artifacts (areas of noisy terrain and spurious spikes) in the DEM in the northwest of zone 1 near the cloudy area and in the south of zone 3 near the Toubkal peak. We manually delineated these erroneous pixels in a GIS software and changed their value to No-data (They represent 2% of the data). These remaining gaps were isolated and covered areas generally smaller than the SRTM pixel size; hence, we filled them using the `gdal_fillnodata.py` utility with a radius of 11 pixels as a maximum search distance (44 m). The final DEM is shown in Figure 2.

To evaluate the DEM accuracy, seven ground control points were collected with a SX Blue dGPS in the Rheraya catchment on 14 May 2015. The mean absolute error in elevation at the ground control points is equal to 4.72 m, and the normalized median absolute deviation (indicator of the random error) is 4.10 m (defined as $NMAD = 1.4826\,\text{median}(|\Delta h_j - m_{\Delta h_j}|)$ where Δh_j refers to the individual errors and $m_{\Delta h}$ denotes the median of errors Höhle & Höhle, 2009). Although higher vertical accuracies can be attained with Pléiades (Berthier et al., 2014; Marti et al., 2015), these results are within the specifications given by Airbus Defense and Space (vertical accuracy inferior to 10 m). To further assess the horizontal accuracy, we used GPS points collected during a 40-km-long road trip with the Sx-Blue device mounted on the roof of the car. The Sx-Blue was set up with an acquisition frequency of one point per second (tracking mode). We superposed these points to the Pléiades orthoimage to verify that the points are aligned with the road (Figure 4). We also digitized several roads sections in different regions from the orthoimage. We found that 90% of the control points collected along these road stretches are within the digitized road polygons. We estimate that roads in this area have a width of 3 to 8 m (Boulaajoul, 2009).

2.2.3. Formosat-2 SCA

The SCA maps were derived from a time series of Formosat-2 images and have a spatial resolution of 8 m. Formosat-2 was launched in 2014 for the purpose of monitoring natural resources, forestry, and environment (Chern & Liu, 2008). Its spatial resolution is respectively 2 m for the panchromatic band and 8 m for the multispectral bands which were used in this research to extract the SCA. Nineteen Formosat-2 images were acquired from February 2008 to June 2009 with a constant view angle over the snow-dominated part of the Rheraya catchment (see the images extent in Figure 5). Fifteen of them are cloud-free and exploitable to derive SCA, which corresponds to an average satellite overpass of 7.5 days, spanning a period starting with an almost completely snow covered scene until complete snow ablation. Images were geometrically corrected by cross correlation with a SPOT (Satellite Pour l'Observation de la Terre) reference image, which was previously georeferenced in the UTM-29N projection system (Marchane et al., 2015). Atmospheric correction was performed with the method of Hagolle et al. (2008) for the retrieval of aerosol optical thickness. Then, the snow-covered masks were computed from a supervised classification based on bands 2 (green), 3 (red), and 4 (near-infrared) using the parallelepiped approach as implemented in the ENVI software (Lillesand, 1979). The training data were sampled in every image separately using three classes: snow, no snow, and shadowed snow (between 5 and 10 polygons of each class for each image). The two snow classes were then

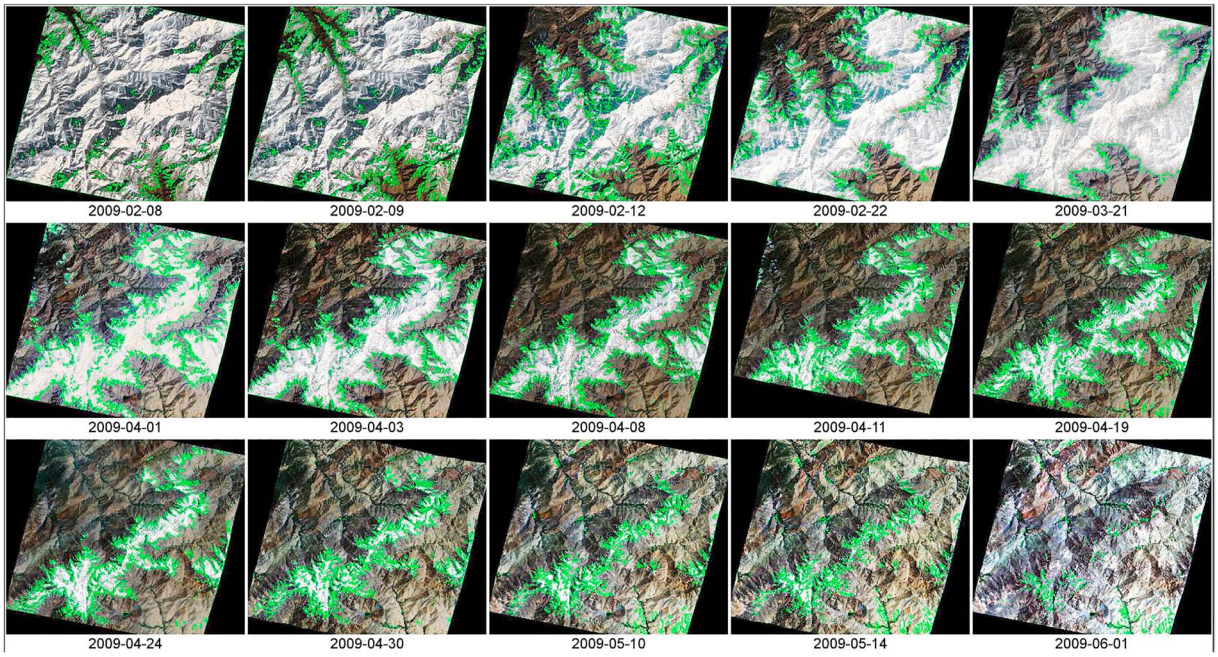


Figure 5. Time series of Formosat-2 images used in this study. The snow cover area derived from the images is represented in green polygons and superposed to natural color composites of the images.

merged in one snow class. The images were visually inspected, and if necessary additional training samples were collected to improve the classification. About 10 samples were used for each date and each class. The accuracy of the results was estimated to exceed 90% for all dates. The only modification made to the data presented in Marchane et al. (2015) is that we refined the geolocalization of the Formosat-2 images stack using the Pléiades orthoimage (section 2.2.2). Indeed, we found a small offset between both data sets in the upper part of the catchment. The correction was done by identifying control points that were visible in both the Pléiades orthoimage and true color composites of the snow-free Formosat-2 images. These reference points were used to fit the parameters of a translation vector, which was then applied to the full Formosat-2 stack. Given the accuracy of the Pléiades orthoimage geolocalization that was estimated above (section 2.2.2), we estimate that the Formosat-2 snow maps of this study have an absolute registration accuracy lower than 8 m. More importantly, the relative coregistration with the Pléiades DEM is lower than 7 m.

This time series of high-resolution SCA maps is unique in the High Atlas. However, it is a precursor of the type of data that will be routinely available when the Sentinel-2 mission will be fully operational (5 days revisit time, cloud permitting). As such, it represents an excellent test bed to test and develop methodologies that will rely on Sentinel-2 data.

2.2.4. Land Cover

The catchment land cover was obtained by a supervised classification of Google Earth Imagery and field observations (Jarlan et al., 2015). The surface was classified in three classes: bare soil (68%), shrubs (29%), and deciduous forest (3%). The land cover map is used in SnowModel to determine various parameterizations linked to the vegetation effects on the snowpack. Here the vegetation has a very marginal effect on the simulations since most of the study domain is classified as bare soil.

3. Methodology

3.1. Model Description and Setup

We used SnowModel, a distributed snowpack evolution model (Liston & Elder, 2006a). SnowModel is composed of four submodels: MicroMet, EnBal, SnowPack, and SnowTran-3D. MicroMet generates a distributed meteorological forcing over the model domain from AWS measurements (Liston & Elder, 2006b). The SnowPack submodel uses the outputs from MicroMet and the energy balance submodel EnBal to simulate the evolution of the height and density of the snowpack (Liston & Elder, 2006a). We used the one-layer option as recommended by the default settings. The SnowTran-3D submodel redistributes the snow depth over

Table 2
Air Temperature Lapse Rates (τ in °C/km) and Precipitation Correction Factors (χ in km^{-1}) Used in This Study

Lapse rate	Jan	Feb	Mar	Apr	May	Jun	Jul	Aug	Sep	Oct	Nov	Dec
τ	4.40	5.90	7.10	7.80	8.10	8.20	8.10	8.10	7.70	6.80	5.50	4.70
χ (AWS)	0.09	0.13	0.00	0.00	0.26	0.05	0.20	0.20	0.20	0.25	0.11	0.17
χ (Formosat-2)	0.12	0.04	0.35	0.31	0.35	0.05	0.20	0.20	0.20	0.22	0.19	0.31

Note. The precipitation factors were first derived from automatic weather station data (AWS) and then optimized using the snow cover area data (Formosat-2).

the terrain depending on wind direction and speed (Liston et al., 2007). However, we did not activate this module for this study due to the lack of in situ wind direction measurements.

The core of the model is based on the resolution of the surface energy balance of the snowpack as implemented in EnBal (Liston & Elder, 2006a).

$$Q_m = (1-\alpha)Q_{si} + Q_{li} + Q_{le} + Q_h + Q_e + Q_c, \tag{1}$$

where Q_{si} (W/m^2) is the incoming shortwave radiation, Q_{li} (W/m^2) is the incoming longwave radiation, Q_{le} (W/m^2) is the emitted longwave radiation, Q_h (W/m^2) is the turbulent exchange of sensible heat, Q_e (W/m^2) is the turbulent exchange of latent heat, Q_c (W/m^2) is the conductive energy flux, Q_m (W/m^2) is the energy flux available for melt, and α is the surface albedo. Q_{li} is computed by taking into account the cloud cover and the elevation (Liston & Elder, 2006b). Q_{li} is estimated by assuming that the snow behaves like a gray body with an emissivity of 0.98 (Liston & Hall, 1995). The turbulent exchange of sensible and latent heat are computed using the bulk equation with a stability correction (Liston & Hall, 1995). The conduction of heat through the snowpack was neglected.

We modified some aspects of MicroMet. Spatial interpolation in MicroMet is based on the Barnes objective analysis scheme, which uses a Gaussian distance-dependent weighting function to interpolate the station data to the regular model grid. Prior to this interpolation, elevation-dependent corrections are applied to remove the effect of elevation on the precipitation, air temperature, and humidity, that is, as if the domain was flat. Once the Barnes interpolation is performed, the data are lapsed back to the grid elevation as given by the DEM. In the case of air temperature, the elevation correction is a linear function of elevation:

$$T_x = T_{stn} - \tau(Z_x - Z_{stn}), \tag{2}$$

where T_{stn} (°C) is the observed station air temperature at Z_{stn} elevation. T_x (°C) refers to the temperature in a given elevation at Z_x. τ is a monthly lapse rate (°C/km) given in Table 2.

To distribute the precipitation over the domain, MicroMet interpolates the observed precipitation by using Barnes objective scheme. Then, it generates a topographic reference surface by interpolating also the elevation of stations. This topographic reference is used to adjust the precipitation with a nonlinear function of elevation difference (equation (3)). The modeled precipitation P_x (mm), at grid point x of elevation Z_x, is equal to

$$P_x = P_0 \times \frac{[1+\chi(Z_x - Z_0)]}{[1-\chi(Z_x - Z_0)]}, \tag{3}$$

where P_0 (mm) is the interpolated precipitation, Z_0 (m) is the interpolated station elevation. χ (km^{-1}) is the precipitation correction factor, also given at the monthly time step (Table 2). Liston and Elder (2006b) provide default values for air temperature lapse rates and the precipitation correction factors. However, the values of air temperature lapse rates were computed for our study area based on AWS observations, by ordinary linear regression using the monthly averages (Table 2). The monthly precipitation correction factors were computed by least squares optimization of equation (3).

MicroMet simulates the incoming shortwave radiation to the surface (Q_{si}) by taking into account the effect of the geometry of the local slope and assuming that the effects of the surrounding topography are negligible (e.g., no casted shadows).

$$Q_{si} = S(\phi_{dir}\cos i + \phi_{dif}\cos Z), \tag{4}$$

Table 3
Snow Model Parameters

Snow model parameters	Value	Unit
Curvature length scale	500	m
Slope weight	0.58	—
Curvature weight	0.42	—
Melting snow cover albedo	0.6	—
Dry snow albedo	0.8	—
Initial snow density	0.3	—

where S is solar beam radiation (1,370 W/m^2; Kyle et al., 1985), Φ_{dir} (W/m^2) is the direct solar radiation, Φ_{dif} (W/m^2) is the diffused solar radiation, Z is the solar zenith angle, and i is the angle between direct solar radiation and a sloping surface.

$$\cos i = \cos B \cos Z + (\sin B \sin Z \cos(\mu - \xi_s)). \quad (5)$$

B is the terrain slope, μ is the solar azimuth, and ξ_s the terrain slope azimuth (with south having zero azimuth). For more details the reader can refer to Liston and Elder (2006b).

When available, MicroMet assimilates shortwave measurements using a direct insertion method: The difference between simulated and observed shortwaves at the meteorological stations is calculated and interpolated to the model grid using the Barnes interpolation scheme; the difference grid is then added to the simulated shortwave radiation. If a meteorological station is located on a grid cell with a high slope value, the simulated incoming shortwave at this station will be affected by the cos B factor. However, incoming shortwave radiation is typically measured in the horizontal plane by pyranometers. For this study it can be problematic since the terrain of the Rheraya catchment is very rugged. For example, Oukaimeden AWS is located near a ski hill. In addition, the local slope can vary significantly depending on the DEM resolution, which could introduce a spurious dependence of the radiation forcing to the input DEM resolution. Therefore, we modified the routine for radiation data assimilation as follows: first, we compute the incoming shortwave radiation for a flat domain. Then, we compute the differences between the simulated and measured shortwave radiation at the stations. These differences are distributed using the Barnes analysis and added to the shortwave radiation grid which is computed using the DEM. In this study, only one station has radiation measurements; therefore, the Barnes interpolation is skipped and the difference is distributed uniformly over the domain (Liston & Elder, 2006b). This first-order correction assumes that the atmospheric clearness does not depend on the topography.

The wind speed, which influences the turbulent heat exchange, is also modified according to the topography (Liston et al., 2007), but we did not change the associated parameters given that only two AWS measured the wind speed and wind direction was not recorded during the study period.

SnowModel was run at an hourly time step from 1 November 2008 to 10 June 2009. All other parameters were set to default values (Table 3). We performed five simulations by changing only the model resolution (8, 30, 90, 250, 500, and 1,000 m). The Pléiades DEM was resampled using bicubic interpolation.

The resampling resolutions were chosen based on the following considerations: 8 m is the native resolution of Formosat-2; 30 m is the highest resolution that can be theoretically reached from standard DEMs (SRTM and ASTER); 90 m is the highest resolution of current snow reanalyses (Margulis et al., 2015); 250 m is the highest resolution at which the SCA can be extracted from MODIS (Notarnicola et al., 2013a); 500 m is the resolution of the standard MODIS snow product.

3.2. Evaluation of the Simulations

The simulations were evaluated by comparing daily snow depth averages measured at the Oukaimeden AWS, with the simulated snow depth extracted at the corresponding grid cell. The root-mean-square error was used as model verification metric.

We also spatially evaluated the simulations using the Formosat-2 SCA maps. The evaluation domain was defined as the intersection of the Pléiades DEM extent and the Formosat-2 acquisitions extent. We used the simulated SWE to compute the snow presence or absence for each pixel in order to compare the simulations with the binary Formosat-2 snow maps. This conversion of SWE to SCA was done using a constant threshold; that is, for each pixel, if SWE > SWE$_0$, then SCA = 1; otherwise SCA = 0 (Figure 6). We did not use a more complex snow depletion curve formulation (Kolberg & Gottschalk, 2010; Magand et al., 2014; Pimentel et al., 2017b) because these parameterizations introduce more parameters that we are not able to determine in our study area. In addition, parameters of the snow depletion curve are expected to change with the model resolution. To account for the uncertainty in the value of the SWE threshold, we generated the simulated snow maps from a list of 50 equally spaced SWE$_0$ values from 1 to 120 mm water equivalent. This range was chosen based on previous comparison between remote sensing snow maps and station data (Gascoin et al., 2015; Klein & Barnett, 2003). All simulated snow maps were then resampled to the Formosat-2 resolution (8 m) using the nearest-neighbor method (Figure 6). This enabled us to compute a confusion

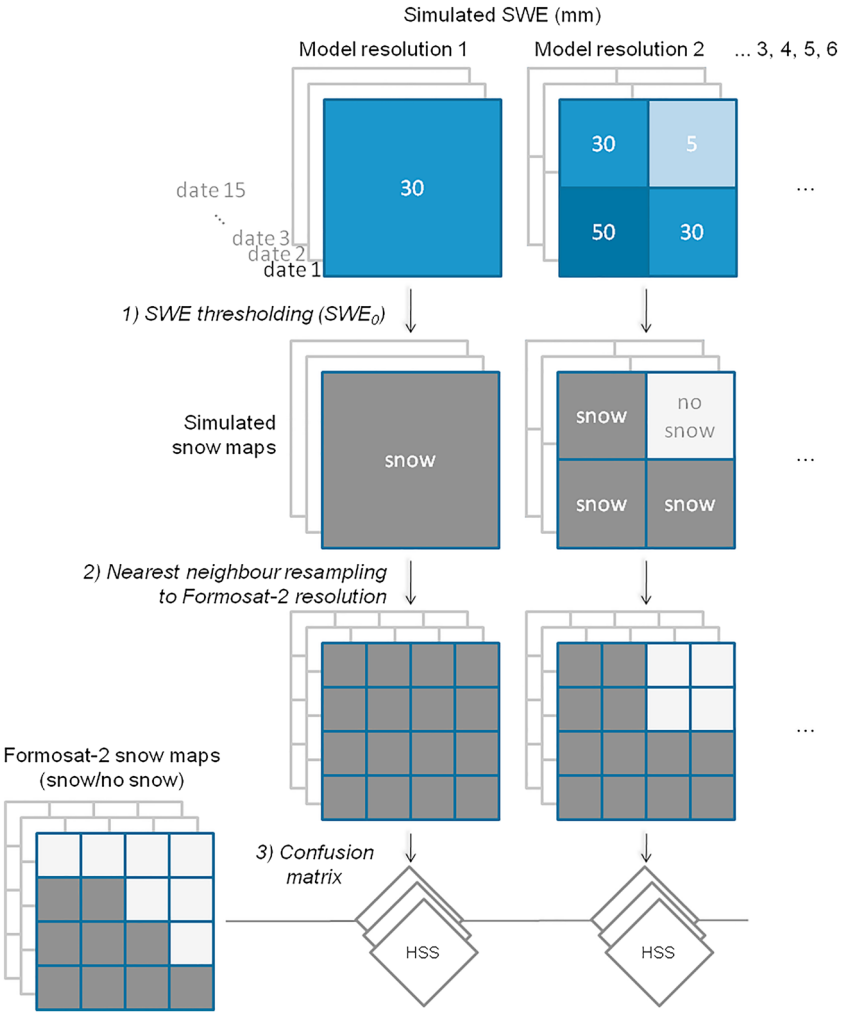


Figure 6. Flow chart of the method used to compute the performance of the model at different resolution based on the Formosat-2 snow maps. The simulated SWE at every Formosat-2 acquisition date was converted to binary snow maps using a SWE_0 threshold. Then, the simulated snow maps were resampled to the same grid as Formosat-2. This enables computation of a confusion matrix between both images, from which we can derive the statistics described in section 3.2. SWE = snow water equivalent; HSS = Heidle skill score.

matrix between each simulated snow map and the corresponding Formosat-2 snow map for each of the 15 acquisition dates.

From the confusion matrix we computed the Heidle skill score (HSS), a statistical index that is recommended when a class is largely dominant (Notarnicola et al., 2013b; our domain is dominated by the snow-free class): $HSS = 2(TP \times TN - FP \times FN)/[(TP + FP) \times (FP + TN) + (TP + FN) \times (FN + TN)]$, where TP (true positive) is the number of cells which were classified as snow in the simulation and the Formosat-2 maps and FP the number of false positives, etc. When a class is dominating, it can be shown that: $\lim_{d\to\infty} HSS = 2TP/(2TP + FP + FN)$ (Notarnicola et al., 2013a). The perfect simulation has an HSS equal to 1, while the worst has an HSS equal to 0.

3.3. Model Calibration

It is important to reduce as much as possible the bias in the model inputs to be able to pinpoint the effect of the model grid resolution. For instance, Baldo and Margulis (2017) used a meteorological data set that was optimized for snowpack modelling from Landsat observations. In our study area, the main source of bias presumably comes from the uncertainty in the distributed precipitation field. We used precipitation data from five stations for a catchment area of 220 km^2. It is by far the highest density of precipitation gauges in the Atlas Mountains. However, there remain large uncertainties on the high elevation precipitation since

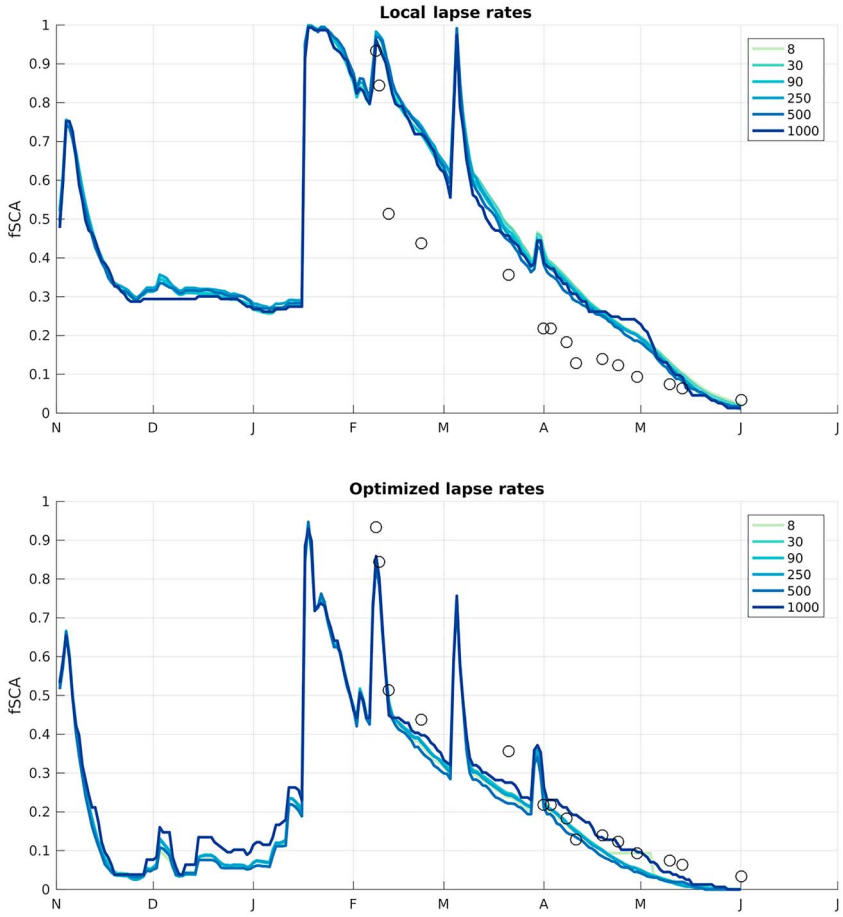


Figure 7. Time series of the snow cover area at each resolution with the default precipitation correction factors (top) and the optimized precipitation correction factors (bottom). The Formosat-2 observations are shown in black circles. The snow cover area is given in fraction of the Rheraya catchment area.

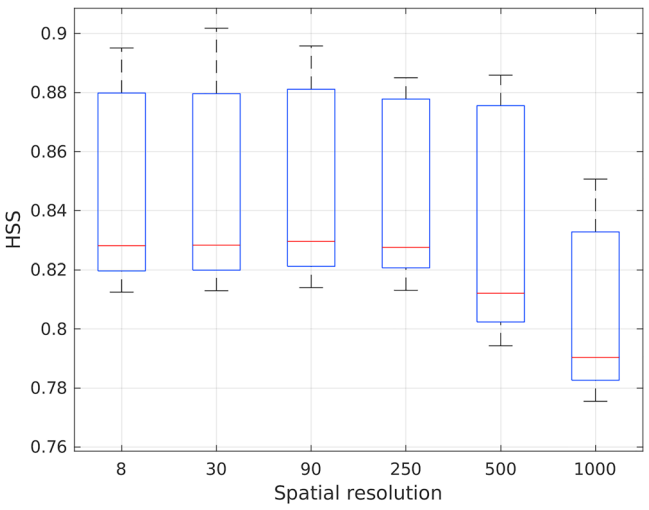


Figure 8. Comparison of the HSS between the simulated and the Formosat-2 snow maps at every resolution. The boxplots show the distribution of HSS for every SWE_0 value and every date (see section 3.2 for details on the method). HSS = Heidle skill score; SWE = snow water equivalent.

the elevation of the highest gauge is 3,230 m asl, while the maximum elevation in the catchment is 4,167 m asl (Table 1). Therefore, we have used the time series of Formosat-2 images to optimize the monthly precipitation correction factors in MicroMet (seven parameters from November to May included). The best correction factors were selected in the interval (0–0.35 km^{-1}) by Monte Carlo sampling using the HSS over the entire study period as optimization variable. The correction factors interval was chosen based on Liston and Elder (2006b). The model was initialized with the correction factors derived from the weather stations (Table 2). Given the large number of model runs that is required for such optimization, we have performed the optimization with the model grid of 250 m (300 model realizations were done). To evaluate the sensitivity of the results to this optimization, we also performed an additional optimization at a resolution of 1,000 m with 150 simulations.

4. Results

4.1. SCA

Figure 7 shows the evolution of the SCA in the Rheraya catchment before and after the optimization of the monthly precipitation correction factors. It shows that the optimization has been successful to reduce a general bias in the model since the evolution of the SCA is closer to the Formosat-2 observations. Note that, in this section, the

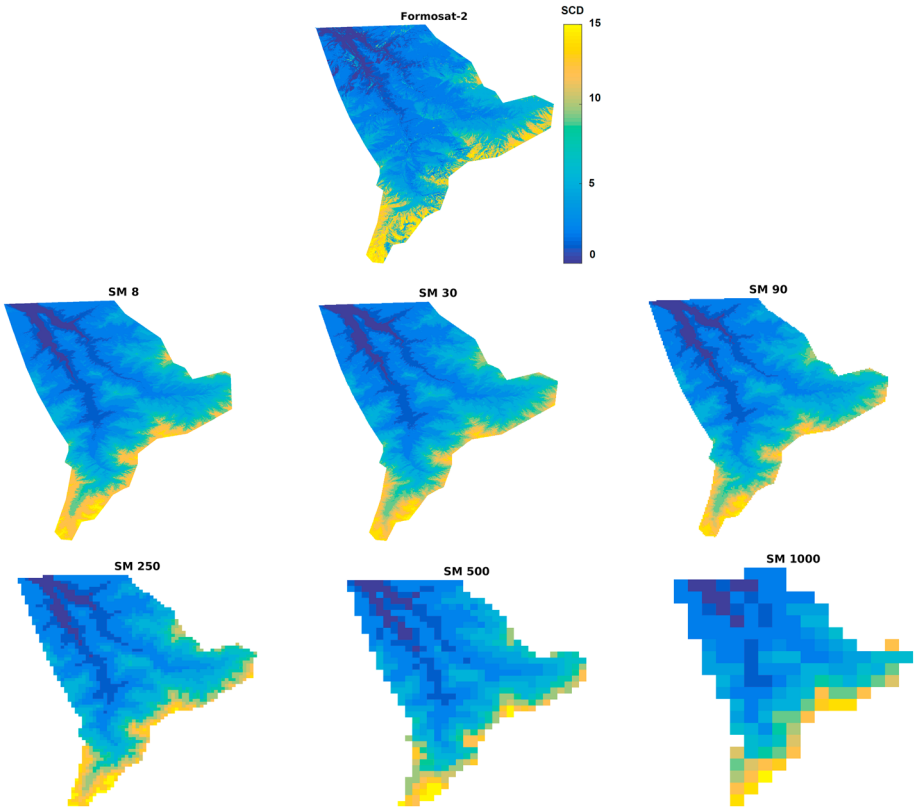


Figure 9. Comparison of the observed number of snow days (Formosat-2) and the simulated number of snow days for each model resolution (SM). The number of snow days (snow cover duration, SCD) was computed using the 15 dates of Formosat-2 acquisitions. All maps are shown with the same color bar in units of days.

results are analyzed using the simulations with the precipitation correction factors that were optimized at 250 m (section 3.3), but we will discuss in section 5 the influence of the resolution at which the optimization was done.

Then, the simulated SCA maps were compared on a pixel basis to the Formosat-2 observations after resampling all the simulated snow maps to 8 m (section 3.2 and Figure 6). This procedure was repeated for every Formosat-2 date and every SWE_0. Figure 8 shows the statistical distribution of the resulting HSS values at each resolution. The differences between the models are low from 8 to 250 m, but the median of the HSS values decreases at 500 m and even more at 1,000 m.

We selected the SWE_0 threshold which gives the highest HSS for each resolution. We did not find a systematic change in the optimized SWE_0. The values for each resolution are (from 8 to 1,000 m): 40, 37, 43, 35, 40, and

Table 4
RMSE of the Simulated Snow Cover Area (SCA, in Fraction of the Catchment Area) With Respect to Formosat-2 Observations and RMSE of the Simulated Snow Depth (SD) With Respect to Oukaimeden In Situ Measurements

Spatial resolution	SCA (%)	SD (cm)
8 m	6.5	30.2
30 m	3.9	30.6
90 m	5.7	30.0
250 m	12.1	30.1
500 m	16.7	47.4
1,000 m	16.9	64.3

Note. RMSE = root-mean-square error.

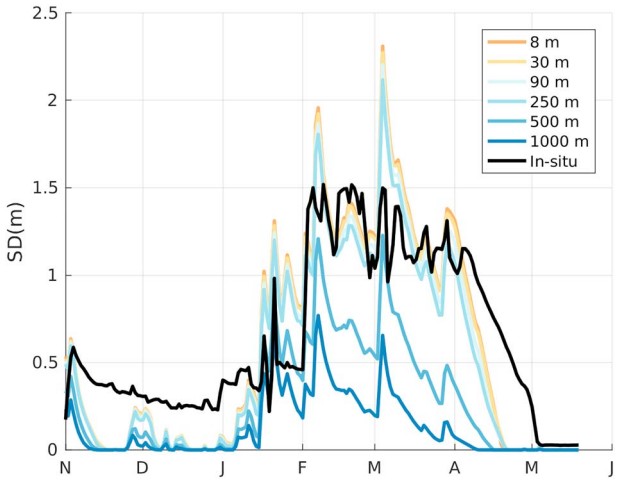


Figure 10. Simulated and measured snow depth at Oukaimeden (from November 2008 to June 2009) for every model resolution. SD = snow depth.

43 mm. We used the average of these SWE_0 values (40 mm) to compute the SCA on every date of Formosat-2 acquisition (15 dates) for all the resolutions. Then, we summed for each pixel the number of days with snow. The same calculation was made with the Formosat-2 data. This comparison shows how coarsening the model resolution modifies the snow patterns at the catchment scale. Simulations from 8 to 250 m produce similar snow cover duration patterns (Figure 9). At 500 and 1,000 m the resolution is too coarse to capture the variability in the snow cover duration that reflects important terrain features like the main valley bottoms. The impact of the resolution is much less visible when the SCA is considered as an aggregated value at the catchment scale (Figure 7); however, the root-mean-square error in the SCA is the largest at the coarsest resolutions, 500 and 1,000 m (Table 4).

4.2. Snow Depth

The comparison with the in situ snow depth record shows that the model captures the main dynamics of the snowpack at Oukaimeden, although there is a consistent overestimation of the ablation rates. The snow depth evolution suggests that this excessive ablation rate was partly compensated by an overestimation of the precipitation. However, simulations from 8 to 250 m are closer to the observations than the 500- and 1,000-m simulations, which exhibit a large negative bias (Figure 10 and Table 4). The large bias at 500 and 1,000 m can be attributed to the smoothing effect of DEM resampling on the elevation of high peaks. Indeed, Oukaimeden AWS is located on an isolated peak (supporting information Figure S1); therefore, the DEM coarsening tends to reduce the elevation at this specific location. The elevation of the Oukaimeden grid cell ranges between 3,238 and 3,231 m in the DEMs at 8 to 250 m resolution, while it is only 3,132 and 2,848 m at 500 and 1,000 m, respectively.

5. Discussion

Changing the model resolution essentially means that we test the model sensitivity to the topographic resolution. Other model parameters may have a much larger impact on the model performance; however, the model resolution has a special interest since it is the parameter that has the strongest impact on the computation time and memory usage. To better understand the effect of the model resolution on the simulations,

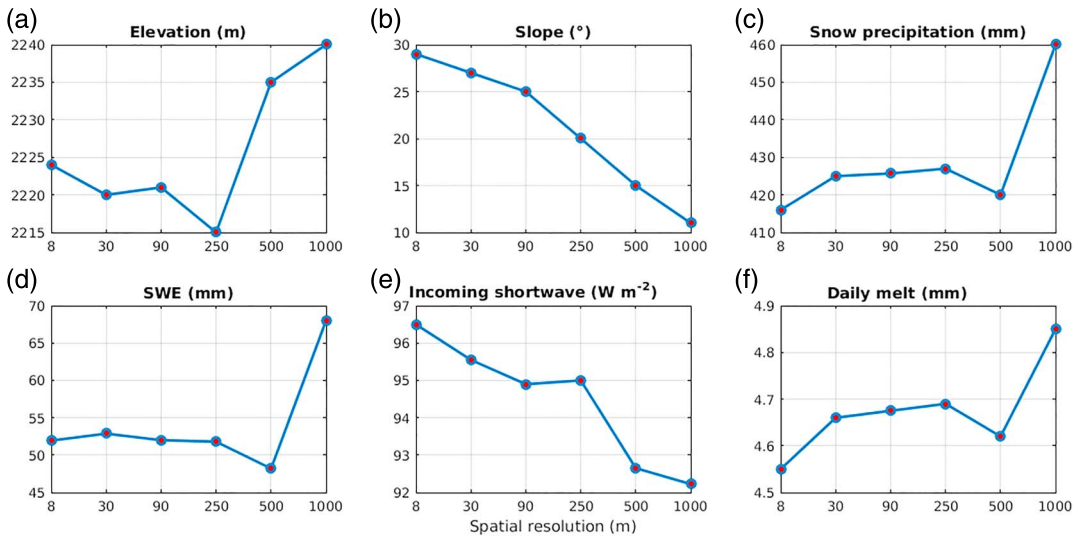


Figure 11. Spatial averages of (a) the model grid elevation, (b) the model grid slope, (c) the total snow precipitation, (d) the mean SWE, (e) the mean incoming shortwave radiation, and (f) the mean daily melt, for each model resolution. These values were extracted from the evaluation area, that is, the intersection of the Formosat-2 extent and the catchment area. SWE = snow water equivalent.

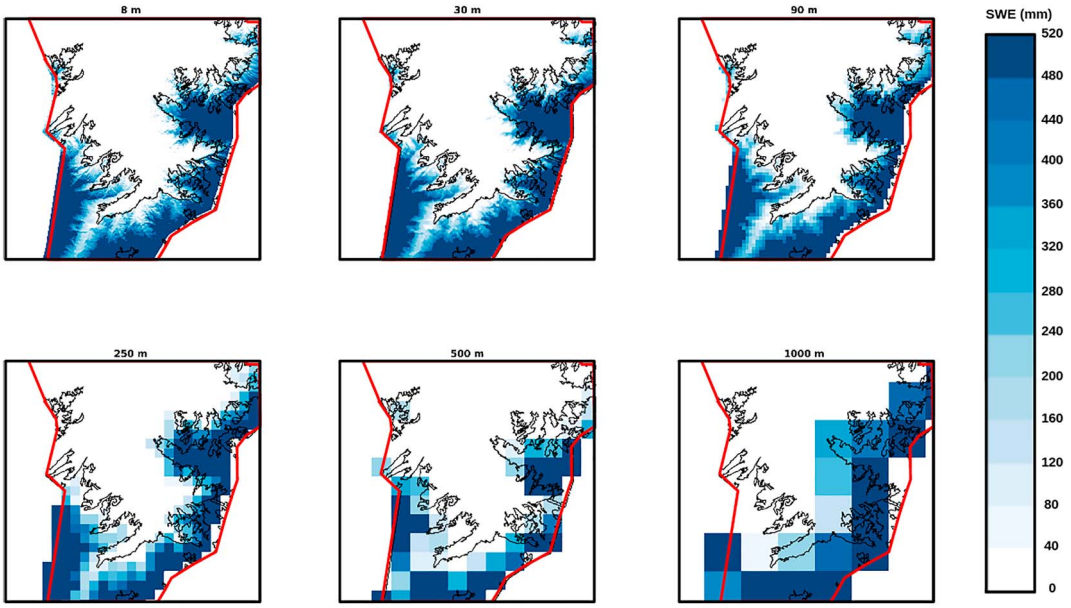


Figure 12. Simulated SWE on 1 April 2009. The black line indicates the extent of the snow cover from the Formosat-2 image acquired on the same day. The red line indicates the model domain boundary. SWE = snow water equivalent.

we have plotted the average of key variables as a function of the model grid cell size (Figure 11). This figure indicates that resampling the DEM from 8 to 1,000 m causes a small change in the average elevation of the evaluation domain since the maximum difference is only 20 (Figure 11). Yet, these mean elevation changes are sufficient to drive a large part model response to the resolution in terms of mass balance mainly because the precipitation increases with elevation (equation (3)).

The effect of the model resolution on the energy balance is more evident on the spatial distribution of the snow cover. We focused on the southern part of the catchment, a high-elevation region where the topography is highly variable with contrasted slopes and aspect. In this area we expect that the meteorological forcing is properly represented given the presence of the Neltner station (Table 1). The spatial distribution

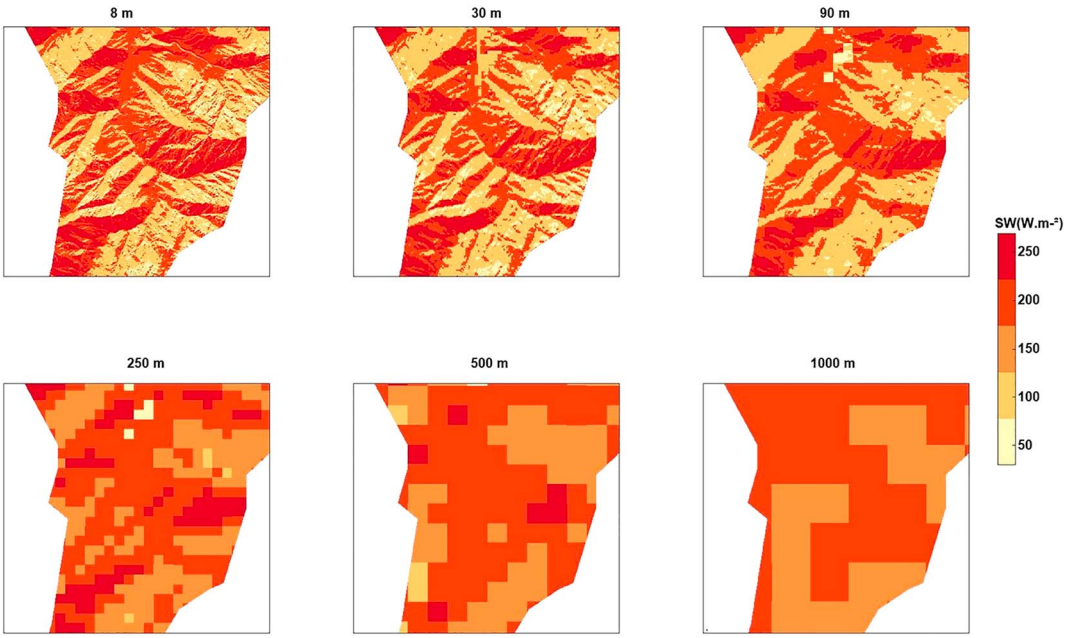


Figure 13. Mean simulated shortwave radiation in the same part of the catchment as Figure 12.

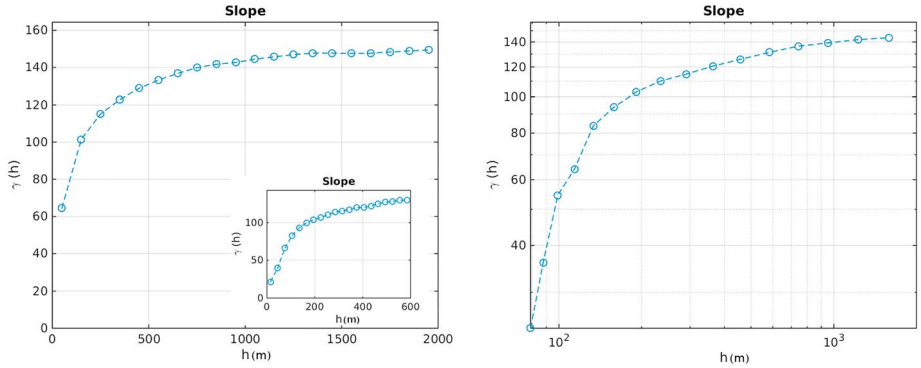


Figure 14. Empirical semivariograms (γ) of the slope from the 30-m ASTER GDEM of the study area (evaluation domain). The semivariograms were computed using 20 bins of distance (h in meters) and a maximum distance of 2,000 m. The inset in the left panel shows the semivariogram with a maximum distance of 600 m. The right panel shows the double logarithmic representation of semivariogram and was computed using log-spaced distance values instead of linearly spaced distance values. Every semivariogram was computed using a subsample of 30,000 randomly drawn points.

of temperature and precipitation is shown in the supporting information (Figure S2). As an example, we selected 1 April to map the SWE at each resolution in this area, and we compared it to the Formosat-2 SCA (Figure 12). It shows that the model is able to capture the spatial variability of the snow cover at the hillslope scale. The SWE is lower in south facing slopes than in north facing slopes. This spatial variability is not inherited from the precipitation forcing since the precipitation variability at this scale in the model is driven by the elevation (equation (3)). Figure 13 shows that the simulated snow patterns in this area are similar to the incoming shortwave radiation. At 250 m and below, the model is able to capture the fact that the slopes of the east-west oriented valleys are not equally snow covered. Above 250 m the model does not capture anymore this slope effect. This observation can be verified on other acquisition dates during the melt season. This can be explained by the fact that the DEM resampling modifies the slope and aspect of the model grid cells, which are used in the calculation of the radiation fluxes (equation (4)). As a result, we can attribute a part of the deterioration of the model performance at 500 and 1,000 m (section 4) to a poorer representation of the radiative forcing on the steepest slopes of the catchment area.

To test the sensitivity of these results to the resolution at which the precipitation correction factors were optimized (section 3.3), we used the precipitation correction factors that were optimized at a resolution of 1,000 m to run the model at each resolution. The results (supporting information Figure S3) show that this optimization has improved the HSS of the 1,000-m simulation as expected (since the precipitation correction factors were optimized at this resolution); however, the HSS remains statistically lower than the HSS of the simulations at 250 m and below. This suggests that the results regarding the sensitivity of the model to the resolution are robust to the resolution at which the optimization of the precipitation correction factor is done. However, it also suggests that the performance of the model might be somewhat overestimated at 250 m in our previous analyses. As a consequence we suggest that an optimal resolution could be found between 250 and 90 m.

Based on these observations, we computed the empirical semivariograms of the DEM slope in the study area. Here, we used the ASTER global DEM V2 rather than the Pléiades DEM, because it is the highest-resolution DEM which is available globally at no cost and thus it could be used to do the same semivariogram analysis in other regions. We find that the semivariogram clearly flattens out at lengths greater than 500 m (Figure 14). The semivariogram computed in the interval 0–600 m further shows that the break is located at 200 m (inset in left panel of Figure 14). In addition, the slope of the semivariogram in the double logarithmic plot has a break near 200 m, which indicates a change in the fractal dimension near this distance.

These values are consistent with our previous findings regarding the effect of the resolution on the snow cover simulation. Indeed, the semivariogram analysis implies that above a grid spacing of approximately 200 m, the variability of the slope is not captured anymore by the DEM. Because the variance of the slope is the main parameter controlling the mean and variance of solar radiation over topographic surfaces

Table 5
Computational Time of the Simulations at Each Spatial Resolution When the Model Is Run on an 800-MHz Processor With 16 GB of Memory

Spatial resolution	Computing time (1 run)
8 m	15 h
30 m	1 h
90 m	8 min
250 m	1 min
500 m	12 s
1,000 m	3 s

(Dubayah et al., 1990; Essery & Marks, 2007; Mckenney, 1999; Pohl et al., 2006), it could also explain why the model performance degrades significantly above 250 m in our case.

6. Conclusion

The objective of this study was to evaluate the performance of a distributed snowpack energy balance model at different resolutions. We applied SnowModel at different resolutions using AWS measurements as input data. We found that the model performed relatively well at resolutions from 8 to 250 m but the performance dropped significantly at 500 and 1,000 m. The same conclusion was drawn from both in situ observations (snow depth at Oukaimeden station) and remote sensing data (Formosat-2 snow maps). However, this conclusion was drawn using precipitation correction factors that were optimized at a resolution of 250 m. An additional experiment using precipitation correction factors optimized at 1,000 m suggests that the optimal resolution is probably between 250 and 90 m. At this level, the choice of the optimal resolution remains subjective since it has to be made based on a trade-off between the accuracy of the simulation and the computational cost of the simulation. Hence, the choice between 90 and 250 m depends on the weight that one would put on each of these two objectives.

Since the Rheraya catchment can be considered as a representative catchment in the snow-dominated areas of the High Atlas, these results suggest that a resolution between 90 and 250 m might be sufficient to simulate the SWE at the scale of the whole High Atlas range, especially in the perspective of a data assimilation scheme based on a particle filter. The reduction of computation time is substantial from 8 to 250 m (Table 5). Current data assimilation schemes typically involve ensembles of 100 simulations (Margulis et al., 2015). Below 250 m, we estimate that the computation times are actually prohibitive given our computer resources for an ensemble-based data assimilation experiment of several snow seasons at the larger scale of the High Atlas Mountains. If computation time is not a limiting factor, we recommend to run the model at 90 m.

The differences in the model outputs are the results of multiple interactions between the DEM and the equations used in MicroMet to spatially interpolate the precipitation, air temperature, humidity, wind speed, and longwave and shortwave radiation. Thus, the results of this study are dependent on this model. However, the main equations used in MicroMet are commonly used to spatially interpolate the meteorological forcing in other models; hence, it is possible that our conclusions remain valid with a different model. We interpret that the main differences are due to the following:

1. The aggregation of the DEM to a coarser resolution tends to reduce the elevation of the highest peaks and to increase the elevation of valley bottoms. The net impact of this DEM smoothing on the snow accumulation is not obvious, however, since it will depend on the mean elevation of the rain-snow transition.
2. The aggregation of the DEM to a coarser resolution tends to decrease the slope of the model grid cells and can change the slope orientation (aspect). This modifies the radiative forcing and therefore the snow cover patterns during the melt season.

The results of this study must be taken with caution since there remain large uncertainties in the model input and output, and also because some topography-dependent processes were not taken into account such as the transport of the snow by the wind (due to a lack of wind observations) or avalanches (due to a lack of model parameterization). Given that the model outputs were mainly evaluated using maps of the SCA during the melt season, the results may be more influenced by the ablation processes. Different results could be obtained if the focus is on accumulation processes. In this case, distributed snow depth data (e.g., Lidar surveys) should be used to evaluate the variations of snow depth during the accumulation season. However, preliminary tests, using wind data from a climate model reanalysis, indicated that the simulated wind transport is low in the study area. Indeed, in SnowTran-3D the wind transport occurs when the surface friction velocity exceeds a threshold value, which depends on the snow density (Liston & Sturm, 1998). In the High Atlas, the snowpack temperature stays close to 0 °C; melt events are common during the accumulation season, and thus, the surface snow density increases rapidly, which inhibits the wind transport. Another limitation of the model is the lack of a casted shadow algorithm. We estimate that the additional fraction of

the catchment area that would be in the shadow if such algorithm was implemented is 23% at 10:00, 4% at 12:00 LT, 0.1% at 14:00, 0.3% at 16:00, and 21% at 20:00 local time. Further work is necessary to evaluate the impact of this deficiency on the snow cover simulation. More advanced radiation schemes are available to improve the spatial interpolation of the radiation in complex terrain (Aguilar et al., 2010). Finally, an important limitation is that the study is limited to a single snow season, while the study area is characterized by a strong interannual climatic variability. High-resolution satellite time series such as the one used in this study are not yet available over multiyear periods, but the advent of the Sentinel-2 mission will change this status quo and will provide more opportunities to address this issue.

Despite these limitations, we found that the model results are consistent with a semivariogram analysis of the DEM of the study area, since the semivariogram of the slope exhibits a break near 200 m. This result, in agreement with previous studies (Essery & Marks, 2007), suggests that a similar semivariogram analysis could be performed in other study areas as a guide to determine the model resolution. Further work is needed to confirm if this recommendation holds in regions with distinct climate and topography, but we expect that similar result could be derived in semiarid mountain regions where the incoming solar radiation is a key factor in the snowpack dynamics.

Acknowledgments
This study was supported by the CNES TOSCA program. M. W. Baba had a doctoral grant funded by the CNES and the Région Occitanie (formerly Midi-Pyrénées). The Pléiades images acquisition was supported by the CNES through the ISIS program. The field work was funded by Agence Universitaire de la Francophonie through the NivAtlas project. We also acknowledge the Laboratoire Mixte TREMA for logistic and financial support. We thank Bastien Richard and Iñigo Irarrázaval for their participation in the GPS survey. We thank G. E. Liston for sharing the SnowModel code and his advices. The station data, the Formosat-2 snow maps, and the GPS data used in this study are available under a Creative Commons Attribution Share-Alike 4.0. license (Baba et al., 2018). The Pléiades data are commercial data that can be obtained via the website (http://www.intelligence-airbusds.com/geostore/). Academic access exists through ISIS (http://www.satelliteimageaccess.teledetection.fr/). Interested readers should contact the corresponding author to request a specific agreement with CNES. We are grateful to Jessica Lundquist (Editor), Nick Rutter (Associate Editor), and the anonymous reviewers who provided many insightful comments that helped improve the quality of the paper.

References

Aguilar, C., Herrero, J., & Polo, M. J. (2010). Topographic effects on solar radiation distribution in mountainous watersheds and their influence on reference evapotranspiration estimates at watershed scale. *Hydrology and Earth System Sciences*, *14*(12), 2479–2494. https://doi.org/10.5194/hess-14-2479-2010

Arola, A., & Lettenmaier, D. P. (1996). Effects of subgrid spatial heterogeneity on GCM-scale land surface energy and moisture fluxes. *Journal of Climate*, *9*(6), 1339–1349.

Baba, M. W., Gascoin, S., Kinnard, C., Marchane, A., Hanich, L., & Hagolle, O. (2018). Snow dataset for the Rheraya catchment (Morocco) (2008–2009). https://doi.org/10.5281/zenodo.1159014

Baldo, E., & Margulis, S. A. (2017). Implementation of a physiographic complexity-based multiresolution snow modeling scheme. *Water Resources Research*, *53*, 3680–3694. https://doi.org/10.1002/2016WR020021

Barry, R. G. (1992). *Mountain weather and climate*. London: Psychology Press.

Berthier, E., Vincent, C., Magnússon, E., Gunnlaugsson, Á., Pitte, P., Le Meur, E., et al. (2014). Glacier topography and elevation changes derived from Pléiades sub-meter stereo images. *The Cryosphere*, *8*(6), 2275–2291.

Blöschl, G. (1999). Scaling issues in snow hydrology. *Hydrological processes*, *13*(14-15), 2149–2175.

Boudhar, A., Boulet, G., Hanich, L., Sicart, J. E., & Chehbouni, A. (2016). Energy fluxes and melt rate of a seasonal snow cover in the Moroccan High Atlas. *Hydrological Sciences Journal*, *61*(5), 931–943.

Boudhar, A., Duchemin, B., Hanich, L., Chaponnière, A., Maisongrande, P., Boulet, G., et al. (2007). Analyse de la dynamique des surfaces enneigé,es du Haut Atlas marocain à partir des données SPOT-VEGETATION. *Science et changements planétaires/Sécheresse*, *18*(4), 278–288.

Boudhar, A., Duchemin, B., Hanich, L., Jarlan, L., Chaponnière, A., Maisongrande, P., et al. (2010). Long-term analysis of snow-covered area in the Moroccan High-Atlas through remote sensing. *International Journal of Applied Earth Observation and Geoinformation*, *12*, S109–S115.

Boudhar, A., Hanich, L., Boulet, G., Duchemin, B., Berjamy, B., & Chehbouni, A. (2009). Evaluation of the snowmelt runoff model in the Moroccan High Atlas Mountains using two snow-cover estimates. *Hydrological Sciences Journal*, *54*(6), 1094–1113.

Boudhar, A., Hanich, L., Marchane, A., Jarlan, L., & Chehbouni, A. (2013). Apport des données Formosat2 à la modélisation du contenu en eau du manteau neigeux du Haut Atlas Marocain. *Revue française de photogrammétrie et de télédétection*, *204*, 51–56.

Boulaajoul, B. (2009), pp. 84: Taylor & Francis. Sécurité routiére au Maroc - Bilan et perspectives.

Chaponniere, A., Maisongrande, P., Duchemin, B., Hanich, L., Boulet, G., Escadafal, R., & Elouaddat, S. (2005). A combined high and low spatial resolution approach for mapping snow covered areas in the Atlas Mountains. *International Journal of Remote Sensing*, *26*(13), 2755–2777.

Chehbouni, A., Escadafal, R., Duchemin, B., Boulet, G., Simonneaux, V., Dedieu, G., et al. (2008). An integrated modelling and remote sensing approach for hydrological study in arid and semi-arid regions: The SUDMED programme. *International Journal of Remote Sensing*, *29*(17-18), 5161–5181.

Chern, J., & Liu, Y. (2008). On-orbit SOH monitor of a satellite—A case study of Formosat-2. *Journal of China Institute of Technology*, *38*(1), 187–205.

Dozier, J., Bair, E. H., & Davis, R. E. (2016). Estimating the spatial distribution of snow water equivalent in the world's mountains. *Wiley Interdisciplinary Reviews: Water*, *3*(3), 461–474.

Dubayah, R., Dozier, J., & Davis, F. W. (1990). Topographic distribution of clear-sky radiation over the Konza Prairie, Kansas. *Water Resources Research*, *26*(4), 679–690.

Durand, M., Molotch, N. P., & Margulis, S. A. (2008). Merging complementary remote sensing datasets in the context of snow water equivalent reconstruction. *Remote Sensing of Environment*, *112*(3), 1212–1225.

Essery, R., & Marks, D. (2007). Scaling and parametrization of clear-sky solar radiation over complex topography. *Journal of Geophysical Research*, *112*, D10122. https://doi.org/10.1029/2006JD007650

Fayad, A., Gascoin, S., Faour, G., López-Moreno, J. I., Drapeau, L., Le Page, M., & Escadafal, R. (2017). Snow hydrology in Mediterranean mountain regions: A review. *Journal of Hydrology*, *551*, 374–396.

Freudiger, D., Kohn, I., Seibert, J., Stahl, K., & Weiler, M. (2017). Snow redistribution for the hydrological modeling of alpine catchments. *Wiley Interdisciplinary Reviews: Water*, *4*(5), e1232.

Gagnon, P., Rousseau, A. N., Mailhot, A., & Caya, D. (2013). A Gibbs sampling disaggregation model for orographic precipitation. *International Journal of Applied Earth Observation and Geoinformation*, *22*, 16–26.

Gascoin, S., Hagolle, O., Huc, M., Jarlan, L., Dejoux, J.-F., Szczypta, C., et al. (2015). A snow cover climatology for the Pyrenees from MODIS snow products. *Hydrology and Earth System Sciences*, *19*, 2337–2351.

Gascoin, S., Lhermitte, S., Kinnard, C., Bortels, K., & Liston, G. E. (2013). Wind effects on snow cover in Pascua-Lama, dry Andes of Chile. *Advances in Water Resources*, *55*, 25–39.

Hagolle, O., Dedieu, G., Mougenot, B., Debaecker, V., Duchemin, B., & Meygret, A. (2008). Correction of aerosol effects on multi-temporal images acquired with constant viewing angles: Application to Formosat-2 images. *Remote Sensing of Environment*, *112*(4), 1689–1701.

Hasegawa, H., Matsuo, K., Koarai, M., Watanabe, N., Masaharu, H., & Fukushima, Y. (2000). DEM accuracy and the base to height (*b*/*h*) ratio of stereo images. *International Archives of Photogrammetry and Remote Sensing*, *33*(B4/1; PART 4), 356–359.

Höhle, J., & Höhle, M. (2009). Accuracy assessment of digital elevation models by means of robust statistical methods. *ISPRS Journal of Photogrammetry and Remote Sensing*, *64*(4), 398–406.

Jarlan, L., Khabba, S., Er-Raki, S., Le Page, M., Hanich, L., Fakir, Y., et al. (2015). Remote sensing of water resources in semi-arid Mediterranean areas: The joint international laboratory TREMA. *International Journal of Remote Sensing*, *36*(19-20), 4879–4917.

Jost, G., Weiler, M., Gluns, D. R., & Alila, Y. (2007). The influence of forest and topography on snow accumulation and melt at the watershed-scale. *Journal of Hydrology*, *347*(1), 101–115.

Klein, A. G., & Barnett, A. C. (2003). Validation of daily MODIS snow cover maps of the upper Rio Grande River basin for the 2000–2001 snow year. *Remote Sensing of Environment*, *86*(2), 162–176.

Kolberg, S., & Gottschalk, L. (2010). Interannual stability of grid cell snow depletion curves as estimated from MODIS images. *Water Resources Research*, *46*, W11555. https://doi.org/10.1029/2008WR007617

Kyle, H. L., Hurley, E. J., & Ardanuy, P. E. (1985). The status of the Nimbus-7 Earth-radiation-budget data set. *Bulletin of the American Meteorological Society*, *66*(11), 1378–1388.

Lillesand, T. M. (1979). Remote sensing and image interpretation. "Minimum distance to means classifier". Multispectral Scanning and Spectral Pattern Recognition 463–464.

Liston, G. E., & Elder, K. (2006a). A distributed snow-evolution modeling system (snowmodel). *Journal of Hydrometeorology*, *7*(6), 1259–1276.

Liston, G. E., & Elder, K. (2006b). A meteorological distribution system for high-resolution terrestrial modeling (MicroMet). *Journal of Hydrometeorology*, *7*(2), 217–234.

Liston, G. E., Haehnel, R. B., Sturm, M., Hiemstra, C. A., Berezovskaya, S., & Tabler, R. D. (2007). Instruments and methods simulating complex snow distributions in windy environments using SnowTran-3D. *Journal of Glaciology*, *53*(181), 241–256.

Liston, G. E., & Hall, D. K. (1995). An energy-balance model of lake-ice evolution. *Journal of Glaciology*, *41*(138), 373–382. https://doi.org/10.3189/S0022143000016245

Liston, G. E., & Sturm, M. (1998). A snow-transport model for complex terrain. *Journal of Glaciology*, *44*(148), 498–516. https://doi.org/10.3189/s0022143000002021

López-Moreno, J., Gascoin, S., Herrero, J., Sproles, E., Pons, M., Alonso-González, E., et al. (2017). Different sensitivities of snowpacks to warming in Mediterranean climate mountain areas. *Environmental Research Letters*, *12*(7), 74006.

Magand, C., Ducharne, A., Le Moine, N., & Gascoin, S. (2014). Introducing hysteresis in snow depletion curves to improve the water budget of a land surface model in an alpine catchment. *Journal of Hydrometeorology*, *15*(2), 631–649.

Marchane, A., Jarlan, L., Hanich, L., & Boudhar, A. (2014). Caractérisation de l-enneigement sur l-atlas marocain par le capteur MODIS et relation avec le climat (période 2000–2011). *Revue Française de Photogrammétrie et de Télédétection*, *204*, 13–22.

Marchane, A., Jarlan, L., Hanich, L., Boudhar, A., Gascoin, S., Tavernier, A., et al. (2015). Assessment of daily MODIS snow cover products to monitor snow cover dynamics over the Moroccan Atlas Mountain range. *Remote Sensing of Environment*, *160*, 72–86.

Margulis, S. A., Girotto, M., Cortés, G., & Durand, M. (2015). A particle batch smoother approach to snow water equivalent estimation. *Journal of Hydrometeorology*, *16*(4), 1752–1772.

Marti, R., Gascoin, S., Berthier, E., De Pinel, M., Houet, T., & Laffly, D. (2016). Mapping snow depth in open alpine terrain from stereo satellite imagery. *The Cryosphere*, *10*(4), 1361.

Marti, R., Gascoin, S., Houet, T., Ribière, O., Laffly, D., Condom, T., et al. (2015). Evolution of Ossoue Glacier (French Pyrenees) since the end of the Little Ice Age. *The Cryosphere*, *9*(5), 1773–1795.

Mckenney, D. W. (1999). Calibration and sensitivity analysis of a spatially-distributed solar radiation model. *International Journal of Geographical Information Science*, *13*(1), 49–65.

Molotch, N., Colee, M., Bales, R., & Dozier, J. (2005). Estimating the spatial distribution of snow water equivalent in an alpine basin using binary regression tree models: The impact of digital elevation data and independent variable selection. *Hydrological Processes*, *19*(7), 1459–1479.

Müller, M. D., & Scherer, D. (2005). A grid-and subgrid-scale radiation parameterization of topographic effects for mesoscale weather forecast models. *Monthly weather review*, *133*(6), 1431–1442.

Notarnicola, C., Duguay, M., Moelg, N., Schellenberger, T., Tetzlaff, A., Monsorno, R., et al. (2013a). Snow cover maps from MODIS images at 250 m resolution, Part 1: Algorithm description. *Remote Sensing*, *5*(1), 110–126.

Notarnicola, C., Duguay, M., Moelg, N., Schellenberger, T., Tetzlaff, A., Monsorno, R., et al. (2013b). Snow cover maps from MODIS images at 250 m resolution, Part 2: Validation. *Remote Sensing*, *5*(4), 1568–1587.

Pimentel, R., Herrero, J., & Polo, M. J. (2017a). Quantifying snow cover distribution in semiarid regions combining satellite and terrestrial imagery. *Remote Sensing*, *9*(10), 995. https://doi.org/10.3390/rs9100995

Pimentel, R., Herrero, J., & Polo, M. J. (2017b). Subgrid parameterization of snow distribution at a Mediterranean site using terrestrial photography. *Hydrology and Earth System Sciences*, *21*(2), 805.

Pohl, S., Marsh, P., & Pietroniro, A. (2006). Spatial–temporal variability in solar radiation during spring snowmelt. *Hydrology Research*, *37*(1), 1–19.

Revuelto, J., Azorin-Molina, C., Alonso-González, E., Sanmiguel-Vallelado, A., Navarro-Serrano, F., Rico, I., & López-Moreno, J. I. (2017). Meteorological and snow distribution data in the Izas experimental catchment (Spanish Pyrenees) from 2011 to 2017. *Earth System Science Data*, *9*(2), 993.

Schlögl, S., Marty, C., Bavay, M., & Lehning, M. (2016). Sensitivity of Alpine3D modeled snow cover to modifications in DEM resolution, station coverage and meteorological input quantities. *Environmental Modelling & Software*, *83*, 387–396.

Schulz, O., & De Jong, C. (2004). Snowmelt and sublimation: Field experiments and modelling in the High Atlas Mountains of Morocco. *Hydrology and Earth System Sciences Discussions*, *8*(6), 1076–1089.

Shean, D. E., Alexandrov, O., Moratto, Z. M., Smith, B. E., Joughin, I. R., Porter, C., & Morin, P. (2016). An automated, open-source pipeline for mass production of digital elevation models (DEMs) from very-high-resolution commercial stereo satellite imagery. *ISPRS Journal of Photogrammetry and Remote Sensing*, *116*, 101–117.

Viviroli, D., Dürr, H. H., Messerli, B., Meybeck, M., & Weingartner, R. (2007). Mountains of the world, water towers for humanity: Typology, mapping, and global significance. *Water resources research*, *43*, W07447. https://doi.org/10.1029/2006WR005653

Winstral, A., & Marks, D. (2014). Long-term snow distribution observations in a mountain catchment: Assessing variability, time stability, and the representativeness of an index site. *Water Resources Research*, *50*, 293–305. https://doi.org/10.1002/2012WR013038

Younas, W., Hay, R. W., MacDonald, M. K., Islam, S. u., & Déry, S. J. (2017). ISLAM, and S. J. Déry A strategy to represent impacts of subgrid-scale topography on snow evolution in the Canadian Land Surface Scheme. *Annals of Glaciology*, *58*, 1–10.

Zkhiri, W., Tramblay, Y., Hanich, L., & Berjamy, B. (2017). Regional flood frequency analysis in the High Atlas mountainous catchments of Morocco. *Natural Hazards*, *86*(2), 953–967.